



JOURNAL OF
APPLIED
CRYSTALLOGRAPHY

Volume 54 (2021)

Supporting information for article:

**Quantifying the robustness of the neutron reflectometry technique
for structural characterization of polymer brushes**

**Isaac J. Gresham, Timothy J. Murdoch, Edwin C. Johnson, Hayden Robertson,
Grant B. Webber, Erica J. Wanless, Stuart W. Prescott and Andrew R. J. Nelson**

Quantifying robustness of the neutron reflectometry technique for structural characterization of polymer brushes: Supporting information

Isaac J. Gresham¹, Timothy J. Murdoch^{2,4}, Edwin C. Johnson², Hayden Robertson², Grant B. Webber², Erica J. Wanless², Stuart W. Prescott^{*1}, and Andrew R. J. Nelson³

¹School of Chemical Engineering, UNSW Sydney, NSW 2052, Australia

²Priority Research Centre for Advanced Particle Processing and Transport, University of Newcastle, Callaghan, Australia

³ANSTO, Locked Bag 2001, Kirrawee DC, NSW 2232, Australia

⁴Current address: Department of Chemical and Biomolecular Engineering, University of Pennsylvania, Philadelphia, Pennsylvania 19104, United States

*email: *s.prescott@unsw.edu.au*

Contents

1	Materials	3
2	Nested sampling	4
2.1	Model selection	4
2.2	Stopping criterion	5
3	Prior characterization	6
3.1	Determination of PNIPAM SLD	6
3.2	Characterization of PNIPAM wafer	7
4	Model construction	11
4.1	FreeformVFP parameterization	11
4.2	Line simplification algorithm	12
5	Additional information regarding PNIPAM datasets	13
5.1	Direct comparison of PNIPAM structures produced	13
5.2	Parameter distributions	13
6	Sensitivity to the diffuse tail	18
7	Evolution of posterior probability during sampling	19
8	Definition of χ^2	22

Supporting files can be found on the Zenodo Archive, DOI: 10.5281/zenodo.4361678.

1 Materials

Native oxide silicon wafers (100 mm diameter, 10 mm thick) were purchased from EL-CAT Inc. (USA). Potassium hydroxide (Chem-Supply Pty. Ltd., AR grade) was used during surface preparation steps. Surface functionalization reagents triethylamine (99 %), 2-bromoisobutyryl bromide (>99 %) and (3-aminopropyl)triethoxysilane (>99 %) were purchased from Sigma-Aldrich and used as received. Tetrahydrofuran (Honeywell Burdick and Jackson, >99 %) was dried over 4 Å molecular sieves (ACROS Organics) before use. N-isopropylacrylamide (Sigma-Aldrich, 98 %) was stored below 4 °C and purified by crystallization from hexane prior to use. Polymerization reagents L-ascorbic acid ($\geq 99\%$), 1,1,4,7,10,10-hexamethyltriethylenetetramine (97 %) and copper(II) bromide (99.999 %) were purchased from Sigma-Aldrich and used as received. Methanol (Sigma-Aldrich, anhydrous, 99.8 %) was used as received and MilliQ water (Merck Millipore, 18.2 M Ω cm at 25 °C) was used throughout. Neutron reflectometry (NR) measurements were performed using pre-filtered (0.45 μ m disk filters) deuterium oxide (D₂O) or MilliQ water.

The polymerization was carried out according to the method of Humphreys et al. (2016).

2 Nested sampling

2.1 Model selection

In Fig. 3, the model evidence is shown for increasing numbers of spline knots; the corresponding SLD and reflectometry profiles are shown here in Fig. S1. All SLD profiles match the structure used to generate the reflectometry data, while all models above two knots exhibit equally excellent fits to the reflectometry data.

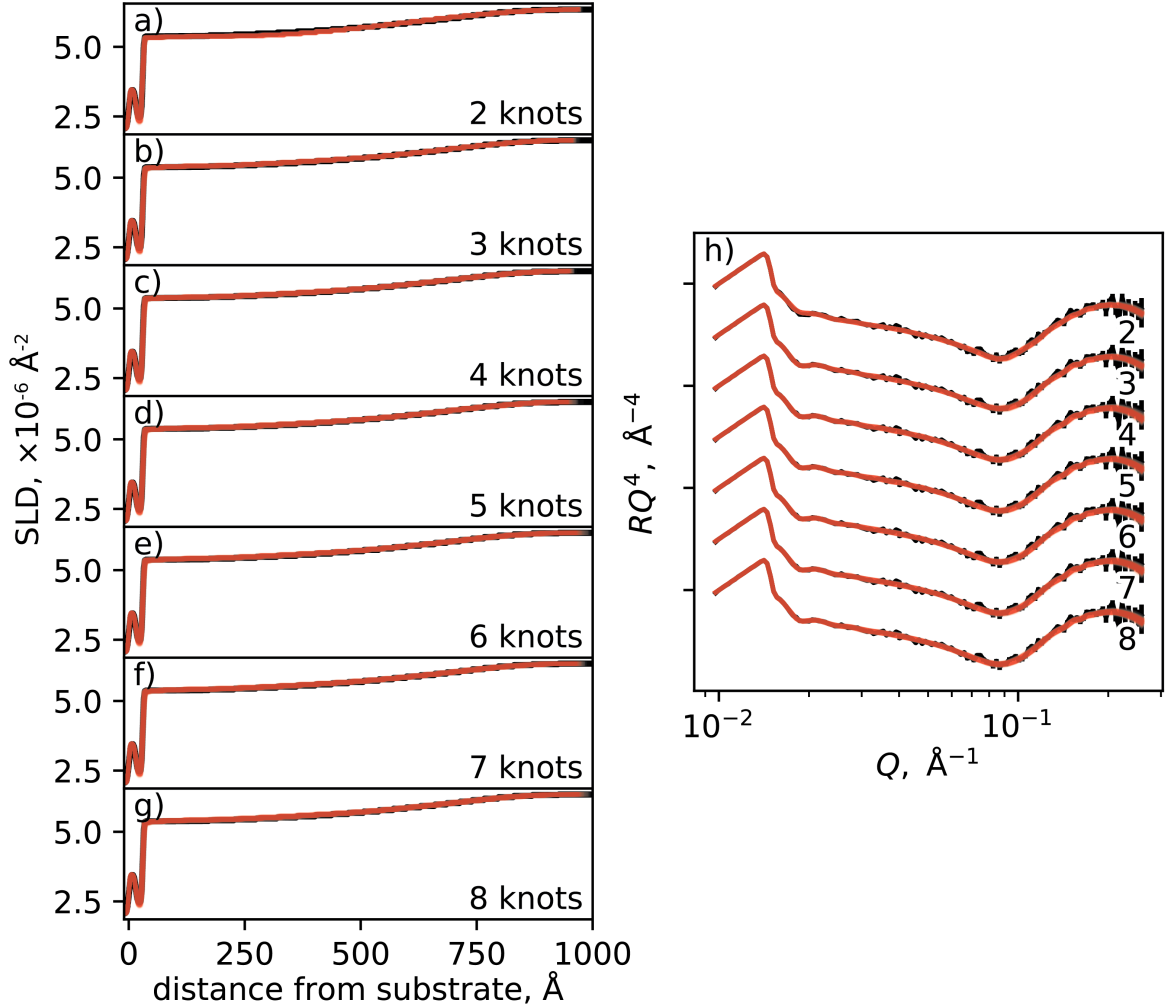


Figure S1: Structural output from the nested sampling process used to estimate the model ratio evidence, corresponding to Fig. 3, processed to be analogous to the output of the MCMC processes used in this work (using `dynesty.utils.resample_equal`). a-g) show that the nested sampler (red) converged on the true structure (black) for all numbers of knots used. (h) Corresponding reflectometry profiles are shown against the simulated data; fit quality is virtually identical for models with more than two knots.

2.2 Stopping criterion

Here we used the default *dynesty* stopping criterion (as of version 1.0.1):

$$\frac{S_p(n)}{0.02} < 1 \tag{S1}$$

where S_p is the posterior stopping function and n is the total number of Monte Carlo realizations used to generate the posterior stopping function (we use $n = 128$, the default value). Here S_p is taken as the fractional sample standard deviation in the approximated Kullback–Leibler divergence.

3 Prior characterization

3.1 Determination of PNIPAM SLD

Widmann et al. (2019) convincingly show that the amide in PNIPAM can become deuterated by exposure to D_2O vapor. This H-D exchange appears to occur over approximately three days at 90 % relative humidity and a temperature of $26.5^\circ C$ (Widmann et al., 2019). It is expected that this H-D exchange would occur faster in a D_2O solution, rather than vapor, but this has not been confirmed.

To measure the SLD of deuterated PNIPAM, we undertook the following experiment. PNIPAM brushes, grown using the grafting-from recipe described above, were created on two 100 mm silicon wafers in identical conditions. These brushes had dry thicknesses of approximately 235 \AA as measured by NR. After an initial measurement in atmospheric conditions, the wafers were immersed in water for three days — one in H_2O and one in D_2O . The wafers were then removed from the water, quickly dried under nitrogen, and placed under vacuum on the *PLATYPUS* beamline. Reflectometry profiles were measured from the wafers at room temperature and 5 mbar of dry air pressure, before the temperature was increased to $50^\circ C$ then $100^\circ C$, where additional profiles were acquired. We conclude that the SLD of pure hydrogenated PNIPAM is $0.72 \times 10^{-6} \text{ \AA}^{-2}$, which corresponds to a theoretical density of 0.973 g cm^{-3} , or a monomer volume of 193 \AA^3 . If the amide proton were to fully exchange using this monomer volume the calculated SLD would be $1.25 \times 10^{-6} \text{ \AA}^{-2}$. The measured SLD of the PNIPAM film soaked in D_2O was $\approx 1.0 \times 10^{-6} \text{ \AA}^{-2}$, which is higher than the hydrogenated SLD, but less than the calculated value for full exchange. We attribute this difference in calculated and measured deuterated SLD to slow exchange kinetics. In the manuscript, the SLD of PNIPAM is allowed to vary between $0.72 \times 10^{-6} \text{ \AA}^{-2}$ and $1.25 \times 10^{-6} \text{ \AA}^{-2}$.

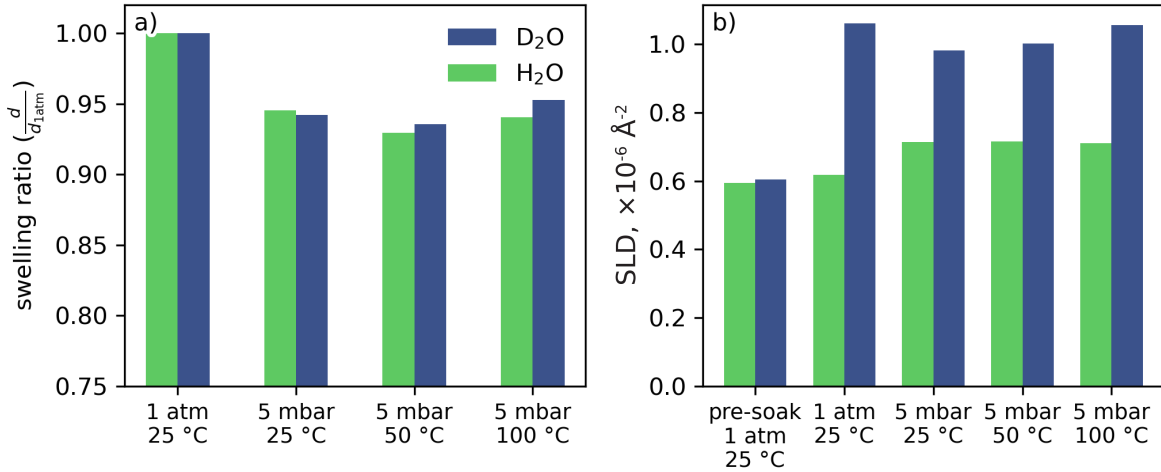


Figure S2: a) Swelling ratio and b) SLD of PNIPAM films in different conditions. The two films had been exposed to liquid H_2O or D_2O for three days before the experiment was conducted. The swelling behavior is similar for H_2O and D_2O , but the layer SLD for the D_2O exposed wafer is significantly higher.

3.2 Characterization of PNIPAM wafer

The brush-coated wafer used for the demonstration of the model was characterized extensively prior to analysis by NR. First, the evenness of the polymer brush coating is confirmed with an ellipsometry map of the surface (Fig. S3), which reveals that the thickness of the area varies between 117 Å and 124 Å. This is an excellent degree of uniformity from a brush synthesis and indicates that the grafting density and molecular weight of the brush is even across the surface. In the situation where uneven coatings are unavoidable, the method detailed in this work can still be applied through incoherent averaging techniques (Johnson et al., 2019).

Fig. S4 shows the result of co-refining (Nelson and Prescott, 2019) data from the PNIPAM brush in air, D₂O at 40 °C, and a PNIPAM contrast-matched H₂O:D₂O mix (CM) at 40 °C. In the CM dataset, the main contribution to the reflectometry profile comes from the native oxide layer, so this contrast is particularly well suited to determining its structure. The D₂O dataset was included to enable the silica layer’s porosity to be determined. Here, the silica layer structure was shared between datasets, allowing the accurate determination of its structure as shown in Fig. S5 and thereby improving the robustness of the method, in particular improving the sensitivity of the analysis to the brush VF profile. In both the CM and D₂O datasets, the collapsed polymer layer was modeled using two slabs, the SLD of which was allowed to vary from 0.72 Å^{-2} to $1.25 \times 10^{-6} \text{ Å}^{-2}$ to account for the deuteration of the amide. Parameters in the different polymer layers were not linked, as the intention was to determine the silica layer structure.

The silica layer structure produced by this process is shown in Fig. S5 and indicates

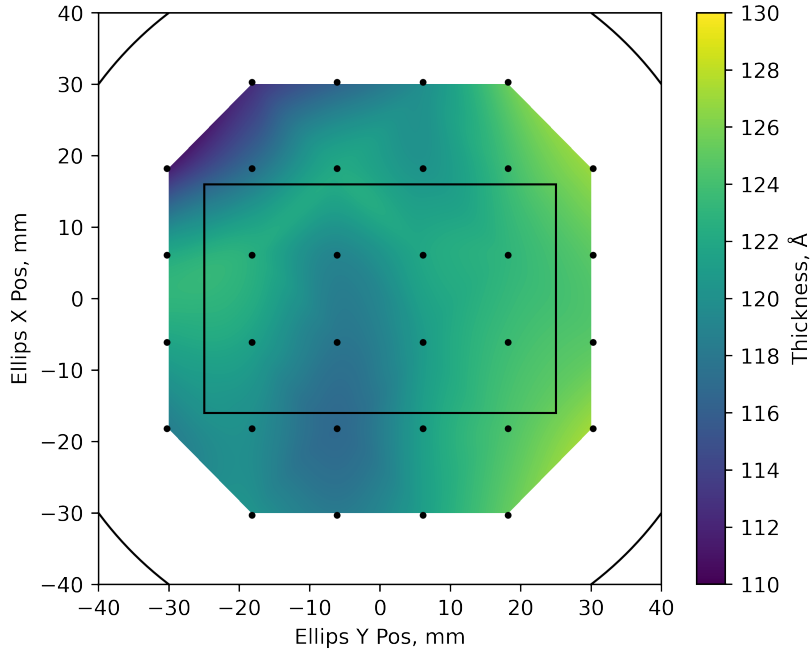


Figure S3: Ellipsometry map of the wafer used. The circle around the perimeter indicates the physical size of the wafer, the 32×50 mm rectangle in the center indicates size and location of the illuminated area in the reflectometry experiment.

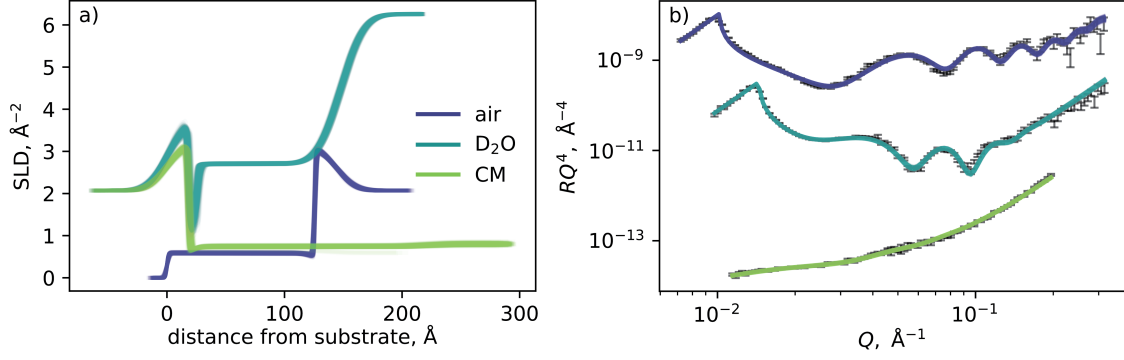


Figure S4: a) SLD profiles and b) corresponding optimized reflectometry profiles used to characterize the silica layer and dry PNIPAM layer thickness. 400 profiles from PT-MCMC sampling are plotted to indicate the narrow spread of viable profiles. Data are from PNIPAM in air at ambient conditions, PNIPAM in D₂O and CM solution at 40 °C.

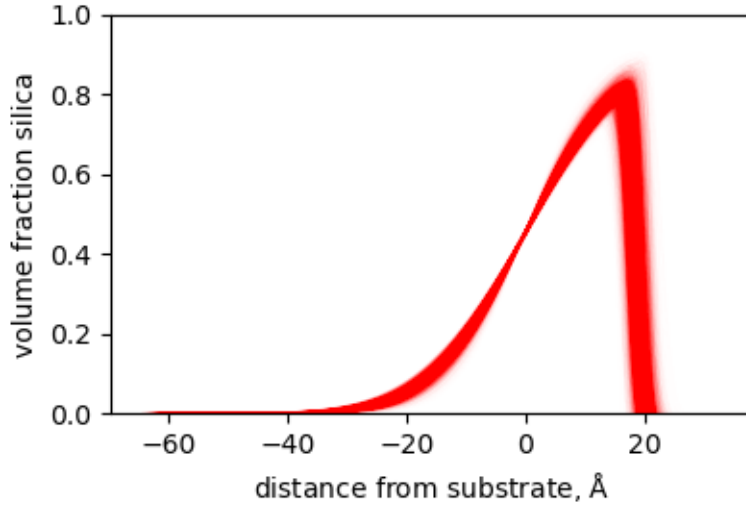


Figure S5: Volume fraction profile of the silica native-oxide layer, derived from characterization shown in Fig. S4. The thickness and SLD distributions are shown below in Fig. S6.

that there is a broad transition between silicon and the native silica layer. Here, the roughness is approximately half the thickness of the oxide layer, which changes the effective SLD of the silica layer. While it would have been possible to constrain the roughness, this would have placed unjustified assumptions on the structure of the silica layer. The interfacial volume is approximated by first determining the fraction of solvent in the dry film, taking the SLD of pure PNIPAM as $0.72 \times 10^{-6} \text{ Å}^{-2}$ and assuming all voids in the film are filled with H₂O. The dry thickness is then multiplied by the polymer fraction in the dry film to yield the interfacial volume (Fig. S7).

PT-MCMC initialized from a prior distribution produced PDFs for hydrated SiO₂ thickness, roughness, SLD, and porosity, (Fig. S5, S6) as well as narrowing our estimate for the interfacial volume of the polymer (Fig. S7). Truncated normal distributions (Fig. S6, S7) with bounds equal to the 95 % confidence intervals were used to encode these values in subsequent analysis.

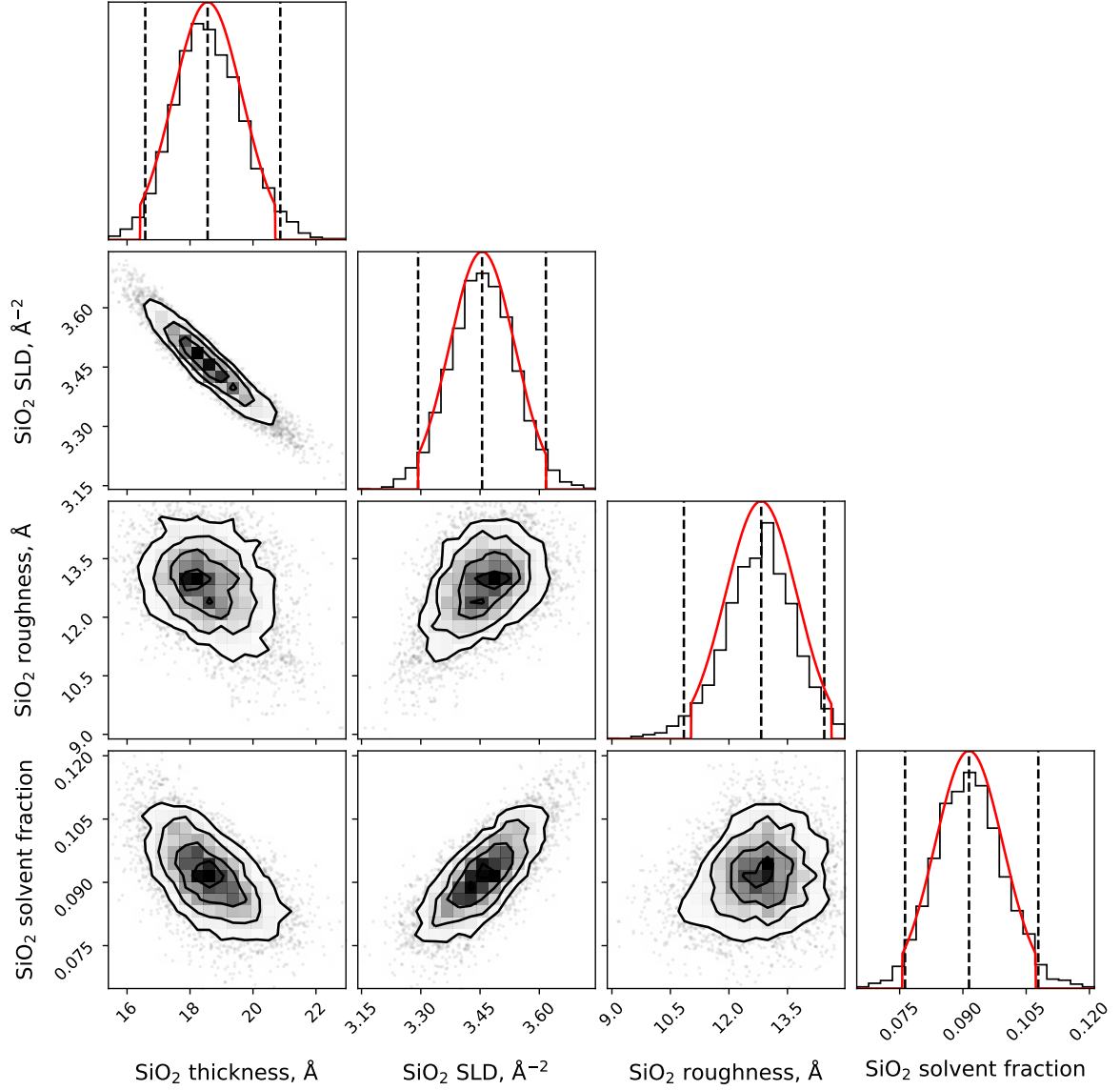


Figure S6: Selected parameter distributions taken from a PT-MCMC treatment of the air-D₂O-CM objective (see Fig. S4). The outermost vertical dashed lines in the plots along the diagonal bound the 95 % confidence interval while the middle indicates the median. The red profiles are the truncated normal distributions used to encode these profiles in the subsequent analysis of the polymer thermoresponse.

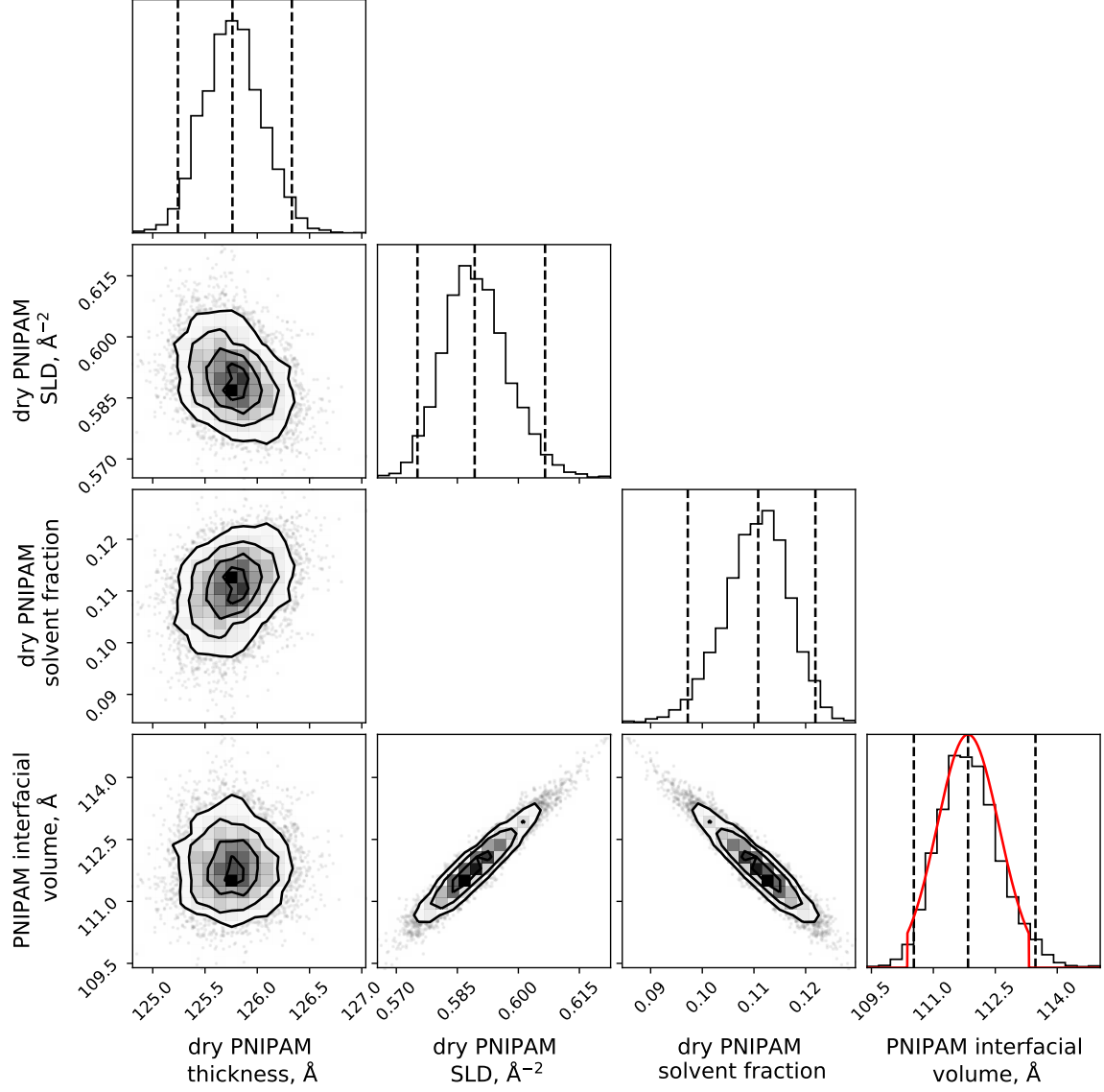


Figure S7: Selected parameter distributions taken from a PT-MCMC treatment of the air-D₂O-CM objective (see Fig. S4). The outermost vertical dashed lines in the plots along the diagonal bound the 95 % confidence interval while the middle indicates the median. The red profiles are the truncated normal distributions used to encode these profiles in the subsequent analysis of the polymer thermoresponse. The correlation plot for the dry SLD and dry solvent fraction has been omitted, as the solvent fraction is calculated from the layer SLD; consequently, the correlation plot includes no meaningful information.

4 Model construction

4.1 FreeformVFP parameterization

The *FreeformVFP* model acts as a wrapper for a PCHIP spline, transforming physically meaningful parameters into a spline. Our approach ensures that the profile can be meaningfully constrained, with only physically allowable profiles being produced. The programmatic implementation can be found in `FreeformVFP.py` (included in the supporting files and also in the `refnx-models` repository¹) and is illustrated in Fig. 1; the full list of parameters as used within the spline and as seen by the user are given in Table S2.

Table S1: Parameter bounds used for solvated sample analyses

parameter	lower	upper
<i>model parameters</i>		
scale factor	0.95	1.05
background	1×10^{-8}	2×10^{-6}
<i>material parameters</i>		
$\rho_{\text{D}_2\text{O}}$	$6 \times 10^{-6} \text{ \AA}^{-2}$	$6.36 \times 10^{-6} \text{ \AA}^{-2}$
ρ_{polymer}	$0.72 \times 10^{-6} \text{ \AA}^{-2}$	$1.25 \times 10^{-6} \text{ \AA}^{-2}$
<i>silica layer parameters</i>		
thickness	†	†
roughness	†	†
VF solvent	†	†
<i>polymer layer parameters</i>		
d_{initial}	5 Å	15 Å
ϕ_{initial}	0.3	0.9
A	†	†
Z_1	0.01	1
f_1	0.15	1
Z_2	0.01	1
f_2	0.15	1
Z_3	0.01	1
f_3	0.15	1
Z_4	0.01	1
f_4	0.15	1

†: parameter constraints are informed by the characterization documented in Section 3.2 and are implemented via a truncated normal distribution (see Figures S6 and S7)

¹User-contributed reflectometry models, `refnx-models`: <https://github.com/refnx/refnx-models/>

Table S2: Relation between the user-facing parameters and those used by the PCHIP splines in *FreeformVFP*

spline	relationship	user
ϕ_{-1}, ϕ_0	$\phi_{-1}, \phi_0 = \phi_{\text{initial}}$	ϕ_{initial}
ϕ_{k+1}, ϕ_{k+2}	$\phi_{k+1}, \phi_{k+2} = 0$	—
\hat{z}_{-1}	$\hat{z}_{-1} = -1.1$	—
\hat{z}_0	$\hat{z}_0 = 0$	—
\hat{z}_{k+1}	$\hat{z}_{k+1} = 1$	—
\hat{z}_{k+2}	$\hat{z}_{k+2} = 2.1$	—
ϕ_i	$\phi_i = \phi_{i-1} f_i$	f_i
E	$E = \frac{A - \phi_{\text{initial}} d_{\text{initial}}}{\int_0^1 \phi d\hat{z}}$	A
\hat{z}_i	$\hat{z}_i = \sum_{l=1}^i \frac{Z_l}{\sum_{j=1}^{k+1} Z_j}$	Z_j

4.2 Line simplification algorithm

The line simplification algorithm employed by *refnx* (based on the algorithm used by Kienzle et al. (2011) in the *Ref1d* package) increases the slab size within the constraint:

$$\text{structure.contract} > (\rho_{\text{max}} - \rho_{\text{min}}) \times (z_{\text{start}} - z_{\text{end}})$$

where **structure.contract** is a tuning parameter that sets a maximum for the product of the slab thickness and the change in SLD from the proceeding slab. For a general overview of simplification methods in reflectometry see the work of Russell (1990). In Fig. S8, **structure.contract** is increased from 0.5 to 20, resulting in more stepped SLD profiles where the freeform curve is discretised into fewer slabs. Fig. S8 shows that values between 1 and 5 do not reduce the validity of the resulting reflectivity profile whilst making a small but significant difference in computation time. Computation time was approximated by measuring the time taken to calculate the reflection produced by the structure in Fig. S8, averaged over 400 iterations. In the analysis of the PNIPAM thermocollapse (Fig. 4), **structure.contract** is set to 1 (corresponding to the dashed line in Fig. S8c), as validity was a higher priority than efficiency.

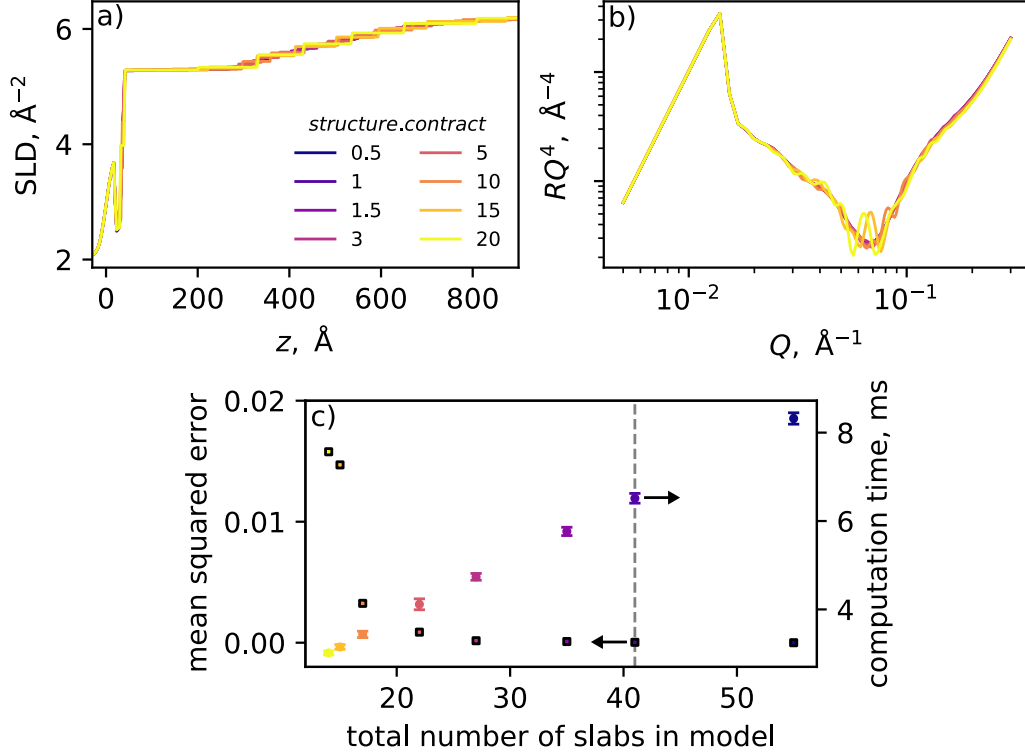


Figure S8: (a) SLD profiles and (b) corresponding reflectometry profiles as the `structure.contract` parameter is increased from 0.5 to 20. The (c, squares) resulting mean squared error (as compared to the `structure.contract` = 0.5 profile) and (c, circles and error-bars) computation time are also shown, plotted against the total number of slabs in the model (which decrease with increasing `structure.contract`). This profiling was performed using version 0.1.16 of *refnx*.

5 Additional information regarding PNIPAM datasets

5.1 Direct comparison of PNIPAM structures produced

The profiles with the highest posterior probability were taken from those shown in Fig. 4 and plotted on the same axes in Fig. S9 for direct comparison. The profiles follow a consistent trend from swollen at low temperatures to collapsed at high temperatures. The reader is referred to the work of Ballauff and Borisov (2016) and Baulin and Halperin (2003) for further discussion of the significance of these structures and their implications for the physical properties of the brush as it undergoes the thermotransition.

5.2 Parameter distributions

The parameter distributions for the polymer parameters are given as histograms in Fig. S10 through S15. We stress that it is the distribution of structures (i.e., volume fraction profiles) that we are interested in, not the distribution of parameters; this is because it is the structures that are of experimental interest and there are possibly multiple parameter configurations that correspond to a single VF profile. Consequently, these parameter distributions are included for the sake of clarity and to allow our method to be more easily

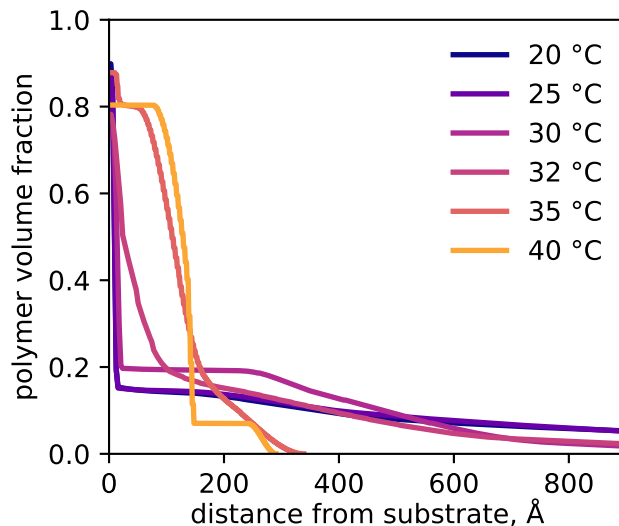


Figure S9: Profiles of best fit taken from Fig. 4, plotted on the same axes for direct comparison.

followed, not because they offer extra information regarding the physical structure of the system.

It should be noted that the posterior distribution for the PNIPAM SLD varies between datasets. Ideally, this value would either be constant or monotonically increasing (as the PNIPAM amide proton is slowly exchanged for deuterium). However, this change in PNIPAM SLD has a minimal effect on the SLD profile produced, being comparable to an uncertainty in the interfacial volume of $\pm 3.5 \text{ \AA}$. SLD and interfacial volume are covariant in this modeling approach, as the same SLD profile can be produced with a lower interfacial volume or a higher polymer SLD. Furthermore, all posteriors have a spread of SLD values across the bounded range. As such, the differences in posterior distribution for the PNIPAM SLD are less than the range which we would expect NR to be sensitive to (for diffuse layers) and have minimal effect on the output of our methodology.

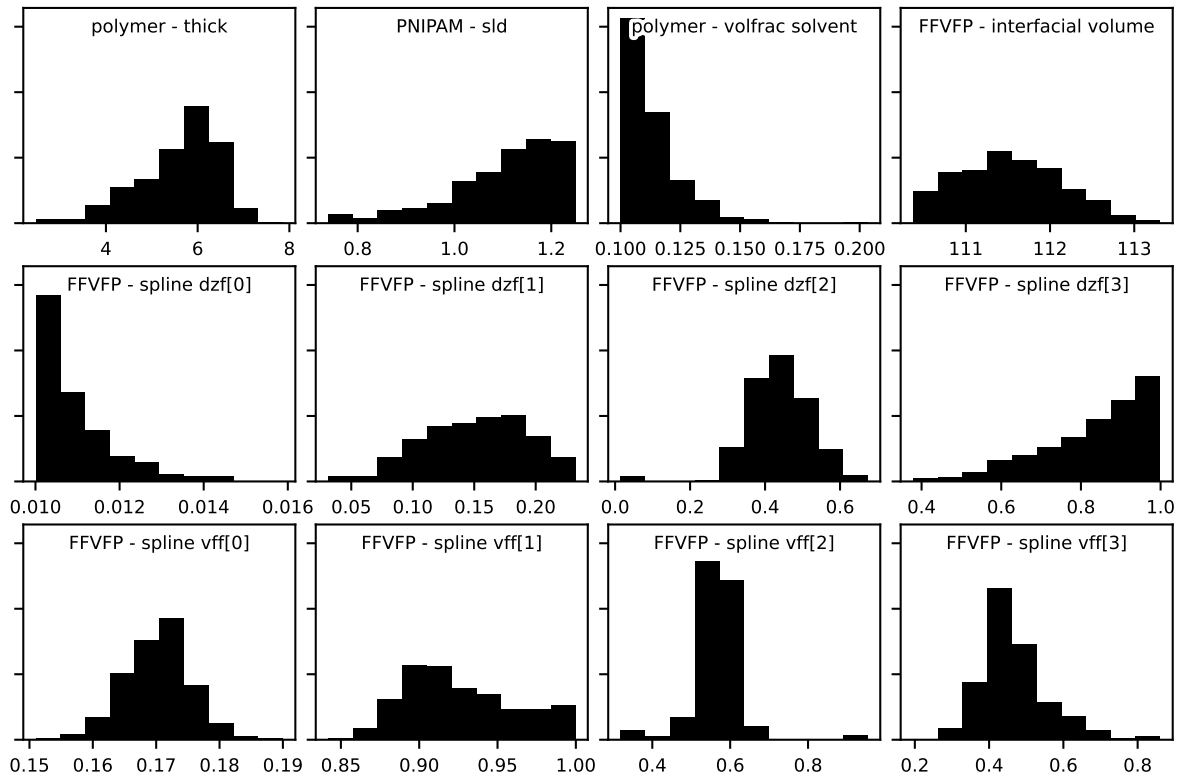


Figure S10: Parameter distributions corresponding to the 20°C dataset in Fig. 4.

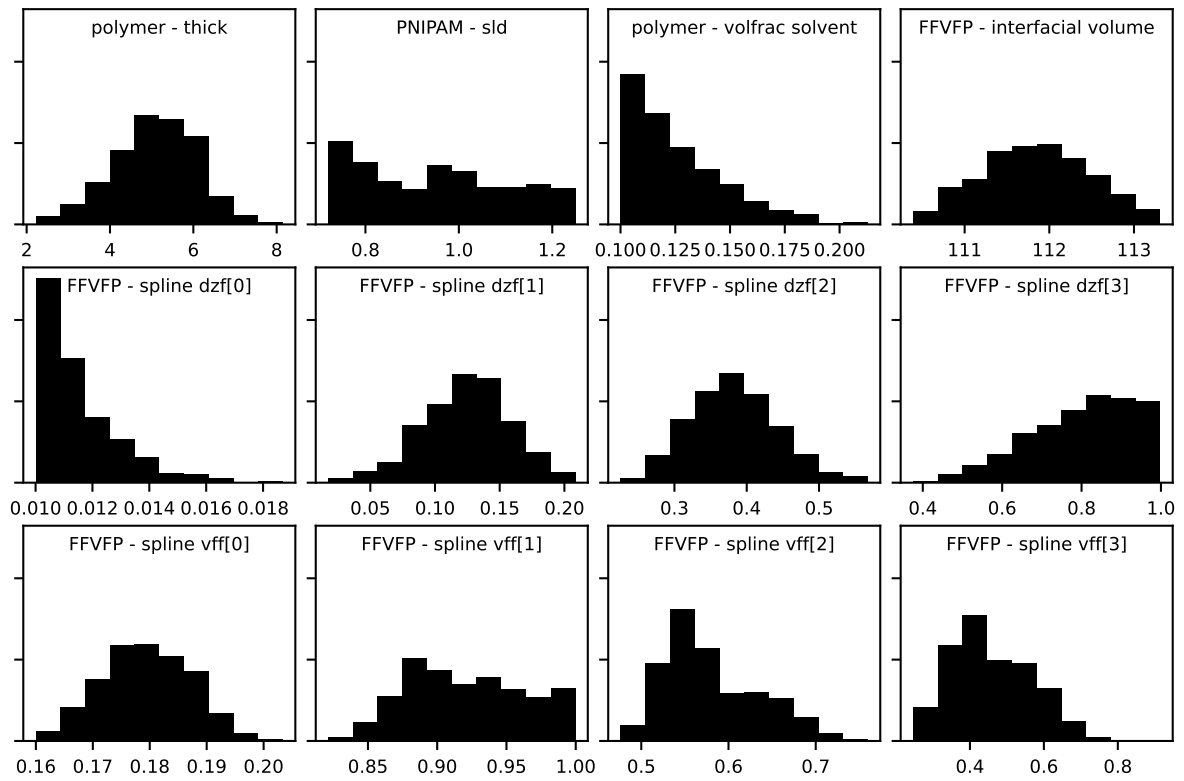


Figure S11: Parameter distributions corresponding to the 25°C dataset in Fig. 4.

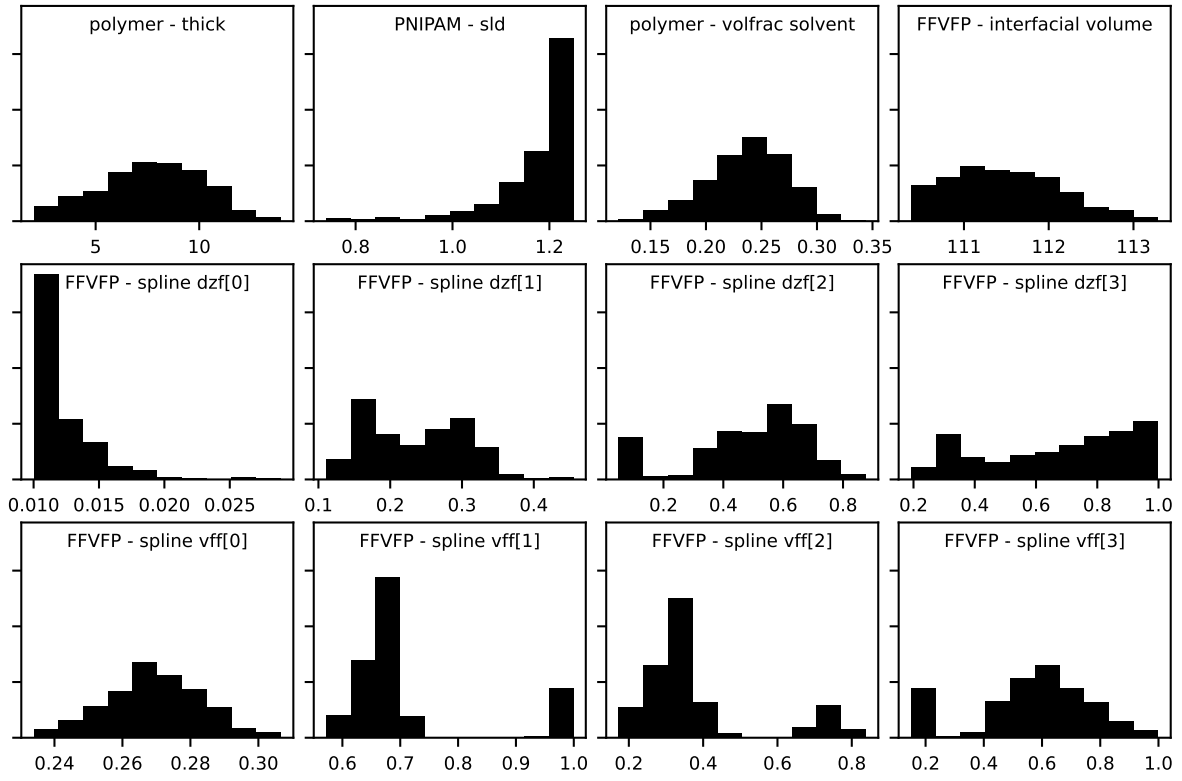


Figure S12: Parameter distributions corresponding to the 30°C dataset in Fig. 4.

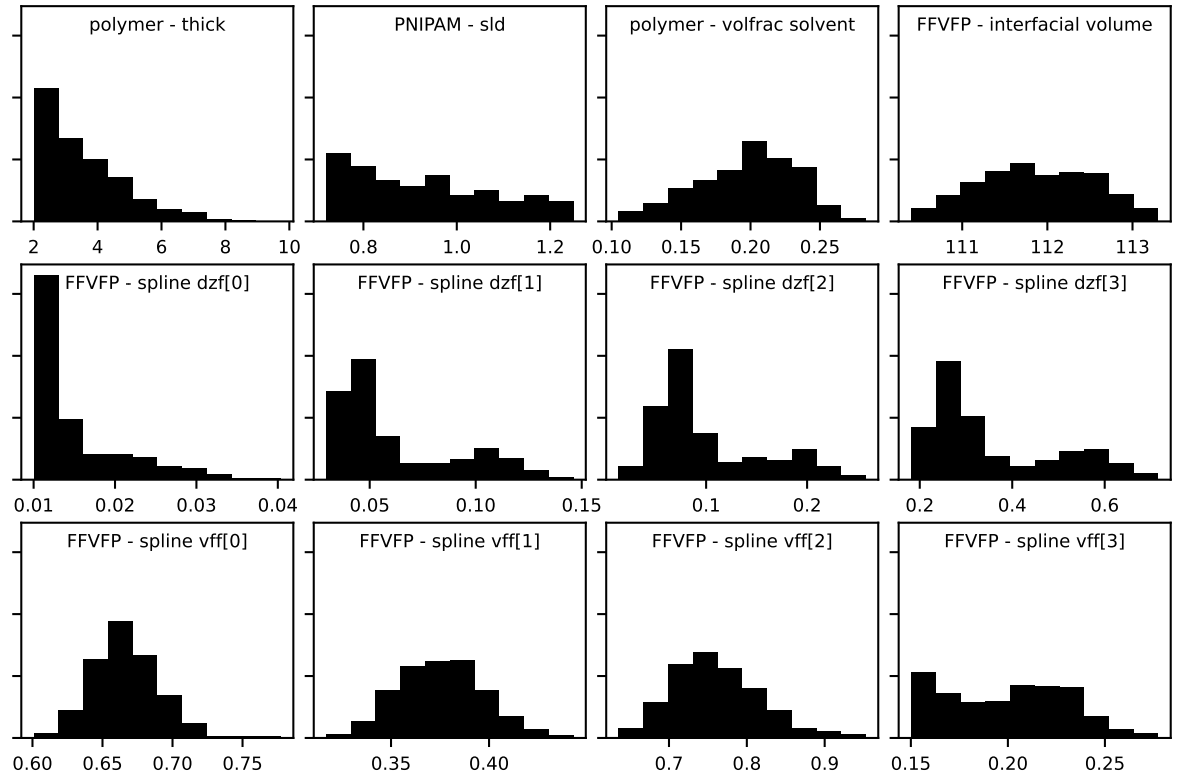


Figure S13: Parameter distributions corresponding to the 32°C dataset in Fig. 4.

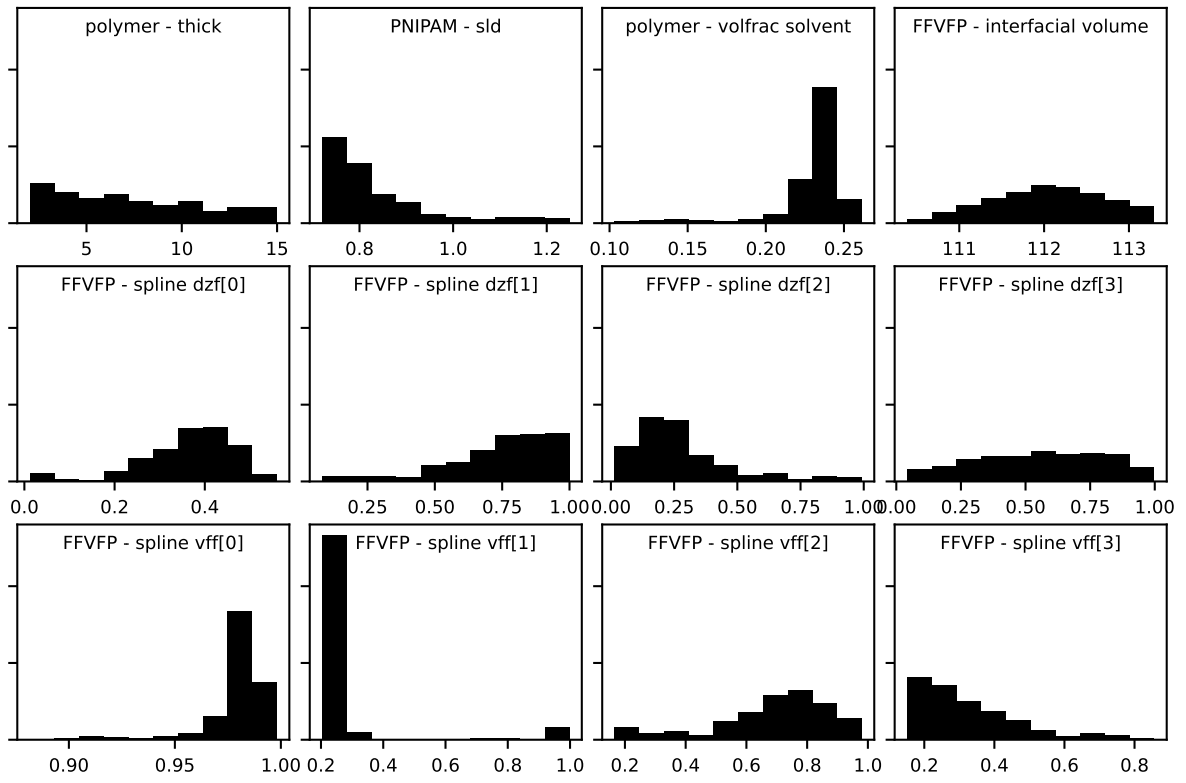


Figure S14: Parameter distributions corresponding to the 35°C dataset in Fig. 4.

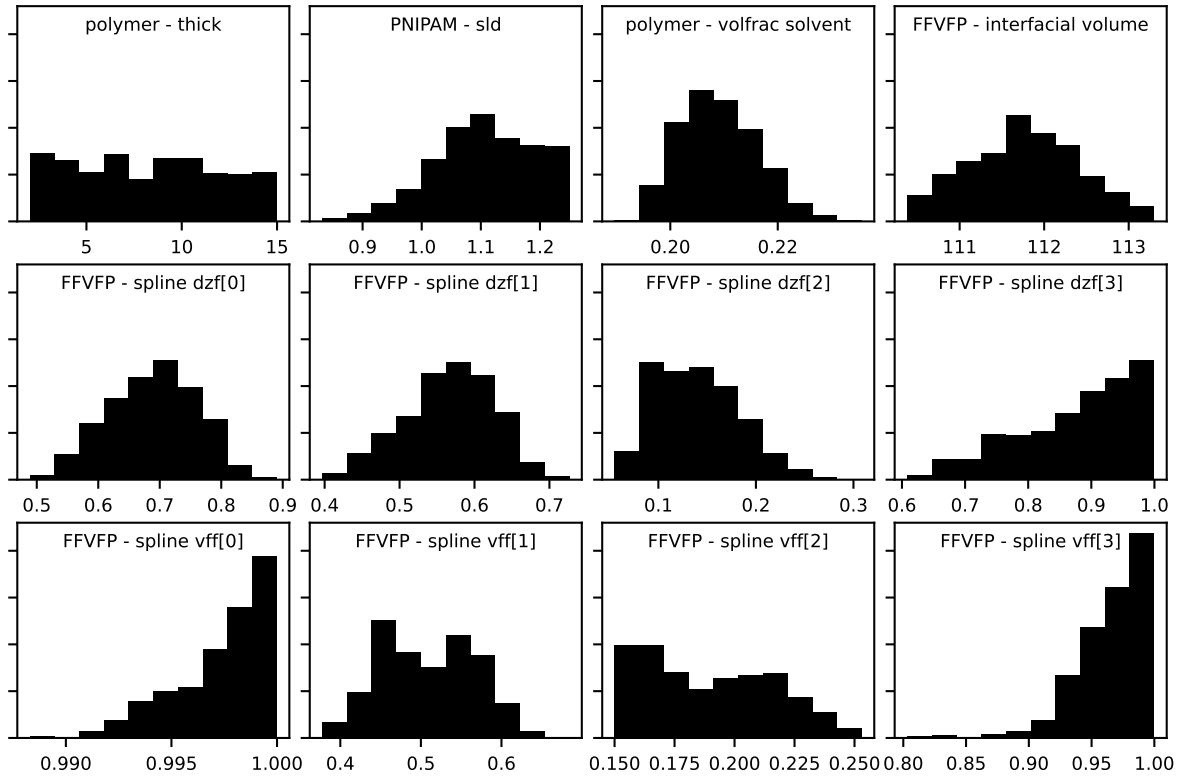


Figure S15: Parameter distributions corresponding to the 40°C dataset in Fig. 4.

6 Sensitivity to the diffuse tail

Extended polymer brushes are extremely diffuse interfaces. The ‘tails’ of these brushes are dilute, with the polymer having a small difference in SLD relative to the solvent, making resolution of tail structure difficult (e.g., Fig. S16). The low-contrast and diffuse structure of these brush tails make their analysis difficult; this is qualitatively shown in Fig. S17a, where structurally distinct profiles produce similar reflectometry profiles. Reflectometry is not totally insensitive to the shape of these tails (e.g., Fig. S17b); however the sensitivity is low and that incorporation of additional constraints (such as the interfacial volume) is important to a successful analysis.

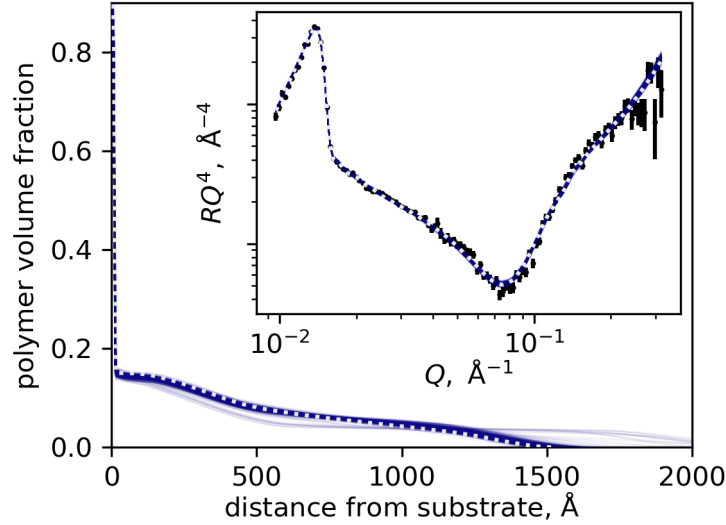


Figure S16: Expanded version of 7a plotted with broader z axis bounds to highlight the spread of profiles that are possible in the tail of the brush. The dashed line corresponds to the differential evolution fit, and is identical to the best fit from PT-MCMC. The reflectometry profile is inset.

Accurately determining and constraining the interfacial volume of polymer aids in an accurate reproduction of the polymer tail. As NR is more sensitive to the higher VF inner region of the brush (i.e., 0 Å to 500 Å in Fig. S17, where the contrast is greater), these will be reproduced accurately, consequently constraining the volume of polymer in the diffuse tail.

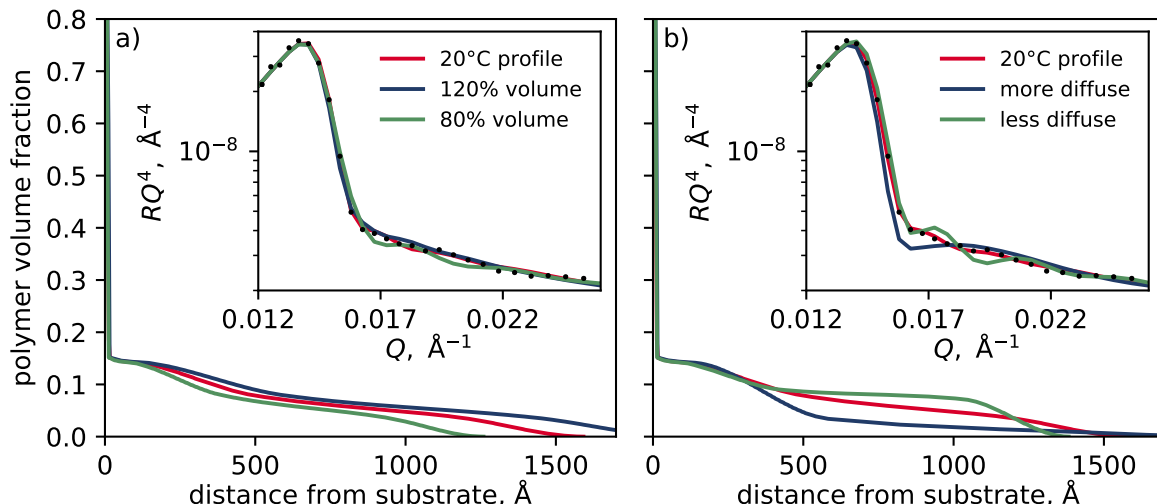


Figure S17: a) profiles with the same shape as the 20 °C profile but different interfacial volumes (produced by scaling the interfacial volume) and b) profiles with the same inner structure but different diffuse decays. Corresponding reflectivity profiles are inset, with the 20 °C data for comparison; the differences between the reflectivity profiles is most distinct at the Q -range shown. While reflectivity is sensitive to the structure of the diffuse structure, the changes in the reflectometry profiles are slight; constraints are necessary to prevent multimodality. One implication of figure a) in particular is that it is important that the interfacial volume of the polymer be correctly constrained.

7 Evolution of posterior probability during sampling

One method for inspecting the progress of an MCMC sampling process is to examine the posterior probability as a function of step number; this gives an indication of the number of modes, their relative probability, and how quickly walkers are migrating between modes. Fig. S18 shows the posterior probability as a function of the step number for the PT-MCMC process that produced Fig. 4 (best achievable fits to the temperature series). Some objectives converge on the optimum rapidly (within ≈ 5000 steps), whilst others have not fully converged by 75 000 steps. In the case of the 30 °C and 35 °C datasets, the optimum is not found until many thousands of steps, while for the 32 °C dataset the apparent optimum is located reasonably rapidly (10 000 steps) but convergence is slow (60 000 steps). From these cases we can conclude that convergence is slower when there are two structures with similar posterior probabilities. Fig. S19 shows the posterior probability as a function of the step number for the PT-MCMC process that produced Fig. 7 (exploration of the impact of constraining the interfacial volume). Convergence is clearly faster for the structures with tighter bounds — a direct result of the smaller parameter space.

The purpose of PT-MCMC sampling here is to give an indication of the families of profiles that match the collected reflectometry data. Specifically, we are interested in the number of profile modes that exist and the distribution of viable profiles around these modes. Given infinite time (that is, when the process is at equilibrium) the distribution of parameters produced by PT-MCMC will converge on the posterior distribution, allowing it to be precisely determined (as we show in Fig. S7 and S6), even for multimodal profiles. However, in most practical instances, a precise approximation of the posterior is not

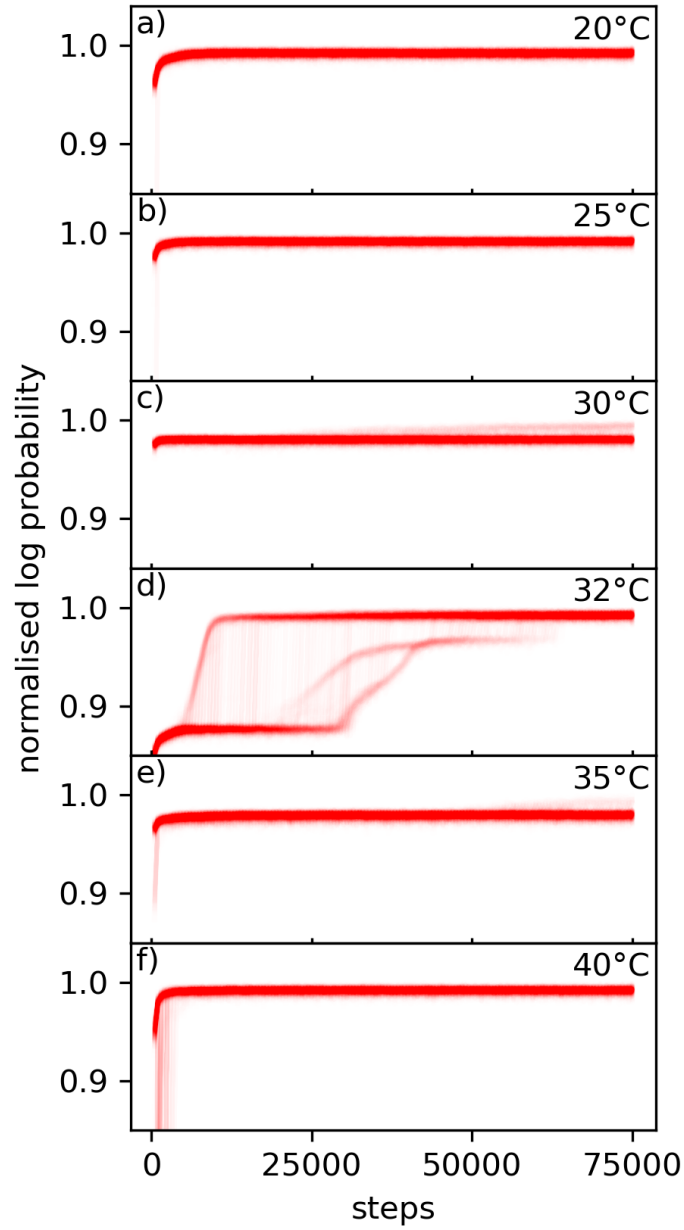


Figure S18: Log probability as a function of step number for the PNIPAM brush at different temperatures, with the position at step number 75 000 corresponding to VF and reflectivity profiles in Fig. 4. Some objectives (a,b) converge on the apparent global optimum rapidly, while others (c,e) exhibit some degree of multimodality, where two structures possess very similar posterior probabilities; the approach to equilibrium here is very slow. Other objectives (d) converge rapidly on a local optimum before locating a better solution.

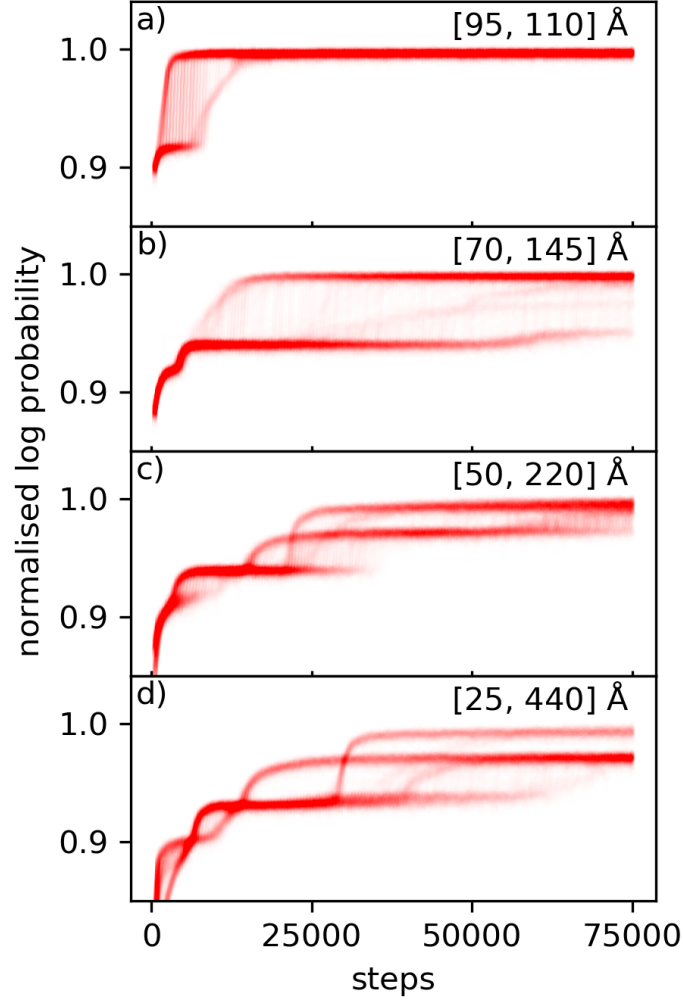


Figure S19: Log probability as a function of step number for broadening interfacial volume constraint, with the position at step number 75 000 corresponding to VF and reflectivity profiles in Fig. 7. Broader bounds appear to increase the number of local optima and increase convergence time. (a) cannot be directly compared to Fig. S18d as the prior bounds were different.

required; it is sufficient to know that a) the experiment is sensitive to the structure of interest and b) what the optimal set/s of parameters are. Fig. S18 shows that some of the profiles in Fig. 4 do not reach equilibrium after 75 000 steps. However, PT-MCMC serves the intended purpose of identifying multimodal solutions. If a detailed posterior probability distribution for the accepted mode is required then point-initiated MCMC can be used to quickly determine the distribution around the mode.

It is worth explaining an apparent contradiction between Fig. S18d and S19a: that the convergence appears faster in Fig. S19a which has a broader interfacial volume prior (a uniform distribution between 100 Å and 115 Å) than in Fig. S18d (a truncated normal distribution between 110 Å and 113 Å). First we must recognize that Fig. S19a is actually multimodal (see Fig. 7a), with both modes having identical prior probabilities, while Fig. S18d is not multimodal. Hence the contradiction can be explained due to the tighter prior in Fig. S18d reducing the posterior probability of one of the modes in Fig. S19a.

8 Definition of χ^2

Where χ^2 is referred to in the manuscript, it is calculated using the following formula

$$\chi^2 = \sum_{n=1}^L \left(\frac{y_n - y_{\text{model},n}}{\sigma_n} \right)^2 \quad (\text{S2})$$

where y_n is the measured data point, $y_{\text{model},n}$ is the corresponding model value and σ_n is the statistical error on y_n .

References

- Ballauff, M. and Borisov, O. V. (2016), ‘Phase transitions in brushes of homopolymers’, *Polymer* **98**, 402–408.
- Baulin, V. A. and Halperin, A. (2003), ‘Signatures of a concentration-dependent flory χ parameter: swelling and collapse of coils and brushes’, *Macromolecular Theory and Simulations* **12**(8), 549–559.
- Humphreys, B. A., Willott, J. D., Murdoch, T. J., Webber, G. B. and Wanless, E. J. (2016), ‘Specific ion modulated thermoresponse of poly(N-isopropylacrylamide) brushes’, *Physical Chemistry Chemical Physics* **18**(8), 6037–6046.
- Johnson, E. C., Murdoch, T. J., Gresham, I. J., Humphreys, B. A., Prescott, S. W., Nelson, A., Webber, G. B. and Wanless, E. J. (2019), ‘Temperature dependent specific ion effects in mixed salt environments on a thermoresponsive poly(oligoethylene glycol methacrylate) brush’, *Physical Chemistry Chemical Physics* **21**(8), 4650–4662.
- Kienzle, P., Krycka, J., Patel, N. and Sahin, I. (2011), ‘Refl1D’.
URL: <http://reflectometry.org/danse>
- Nelson, A. R. J. and Prescott, S. W. (2019), ‘refnx : neutron and X-ray reflectometry analysis in Python’, *Journal of Applied Crystallography* **52**(1), 193–200.
- Russell, T. P. (1990), ‘X-ray and neutron reflectivity for the investigation of polymers.’, *Materials Science Reports* **5**(4), 171–271.
- Widmann, T., Kreuzer, L. P., Hohn, N., Bießmann, L., Wang, K., Rinner, S., Moulin, J.-F., Schmid, A. J., Hannappel, Y., Wrede, O., Kühnhammer, M., Hellweg, T., von Klitzing, R. and Müller-Buschbaum, P. (2019), ‘Hydration and solvent exchange induced swelling and deswelling of homogeneous poly(N-isopropylacrylamide) microgel thin films’, *Langmuir* **35**(49), 16341–16352.